7-2021

Closed-Form Solution for Shock Wave Propagation in Density-Graded Cellular Material Under Impact

Vjendra Gupta

Addis Kidane

Michael A. Sutton
University of South Carolina - Columbia, sutton@cec.sc.edu

Publication Info

Published in *Theoretical and Applied Mechanics Letters*, Volume 11, Issue 5, 2021, pages 100288-.

Theoretical and Applied Mechanics Letters 11 (2021) 100288

Contents lists available at ScienceDirect

Theoretical and Applied Mechanics Letters

journal homepage: www.elsevier.com/locate/taml

Letter

Closed-form solution for shock wave propagation in density-graded cellular material under impact

Vijendra Gupta, Addis Kidane*, Michael Sutton

Department of Mechanical Engineering, University of South Carolina, 300 Main Street, Columbia, SC 29208, USA

ARTICLE INFO

Article history:
Received 21 June 2021
Revised 10 August 2021
Accepted 14 August 2021
Available online 26 August 2021

Keywords:
Functionally graded cellular material
Analytical modeling
Impact response
Closed-form solution
Energy absorption
Density gradient

ABSTRACT

Density-graded cellular materials have tremendous potential in structural applications where impact resistance is required. Cellular materials subjected to high impact loading result in a compaction type deformation, usually modeled using continuum-based shock theory. The resulting governing differential equation of the shock model is nonlinear, and the density gradient further complicates the problem. Earlier studies have employed numerical methods to obtain the solution. In this study, an analytical closed-form solution is proposed to predict the response of density-graded cellular materials subjected to a rigid body impact. Solutions for the velocity of the impinging rigid body mass, energy absorption capacity of the cellular material, and the incident stress are obtained for a single shock propagation. The results obtained are in excellent agreement with the existing numerical solutions found in the literature. The proposed analytical solution can be potentially used for parametric studies and for effectively designing graded structures to mitigate impact.

Cellular materials (CMs) have peculiar properties pertinent to impact mitigation [1,2]. They provide exceptional energy absorption (EA) capability and are used as protection material in dynamic impact applications. They are also extremely lightweight as their solid material is distributed sparsely. They are composed of interconnected cells at the mesoscale level. When a CM is subjected to impact loading, a high-velocity is suddenly imposed at the impact end that causes layer-wise collapse of cells [3]. The progressive collapse of cells advances like a propagating shock and the continuum-based classical shock theory is usually used to model the deformation behavior. The authors in Ref. [3] first applied the shock theory to study the uniaxial dynamic crushing of various wood materials. They obtained an analytical solution for the direct impact scenario, where the CM (wood specimen) moving with a rigid backing mass strikes a stationary surface, assuming a rigid, perfectly plastic, locking (RPPL) material response. Later, the analytical solution for a stationary impact scenario, where a rigid mass moving with an initial velocity strikes a stationary CM, was also developed [4–6]. All the aforementioned studies focused on the response of uniform density CM.

Graded CMs with density variation potentially offer further improvement in the EA performance and crashworthiness, and they have gained attention in recent years [7–14]. Many studies have employed finite element methods to study the response of density-graded CMs subjected to impact loading. Some of the finite element studies have modeled the graded CM as a continuum [7,8], while some other works have made use of cell-based models that concentrate on mesoscale response [15–18]. Although the finite element models seek to capture the material behavior rigorously, they are computationally intensive. There also have been efforts to study the response of the graded CM through experiments, even though manufacturing of continuously graded CMs is challenging. Nevertheless, rapid advancement in manufacturing technology, such as additive manufacturing, has been overcoming this problem [19]. Currently, experimental investigations often approximate the graded structures with multiple uniform density layers of different densities [20–23]. To model continuous density gradation, there have been attempts to take an analytical approach. On this front, initially, a honeycomb structure with a uniform density but a gradient in plateau stress was examined [10]. Although the simplified assumptions in Ref. [10] led to a closed-form solution, the variation in the density was not captured. Thereafter, the density-graded structure was also studied using an analytical approach for the direct impact scenario [24]. Assuming the density of the compacted CM is constant regardless of the initial density, analytical solutions for the shock velocity and the incident stress were obtained for various density profiles in Ref. [24]. There have

* Corresponding author.
E-mail address: kidanea@cec.sc.edu (A. Kidane).

https://doi.org/10.1016/j.taml.2021.100288

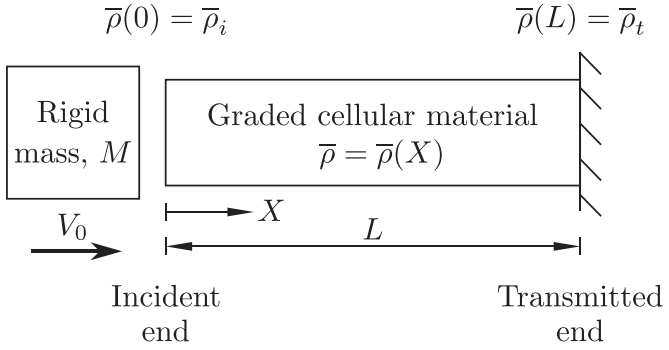

Fig. 1. Schematic diagram of rigid mass striking density-graded CM.

been some works on design strategy to determine the density distribution based on specific crashworthiness requirements [25,26]. Also, several other works [9,11,13] have investigated the stationary impact scenario with a density gradient, but they have used numerical methods for the solution. For better accuracy, numerical methods demand a small step size that results in large number of iterations. A precursory analytical study for density-graded CM under quasi-static loading conditions was performed recently [27]. However, apart from a few attempts discussed above, a general analytical formulation of graded CM under stationary impact scenario does not exist.

In this paper, an explicit and closed-form solution for the stationary impact scenario of density-graded CM is proposed based on the RPPL material model. The solution is facilitated by using the shock front position as an independent variable in the governing shock equations. The effect of density gradation on the total energy absorbed and incident stress is presented. The scope of the study is limited to a linear density variation and a single compaction shock front. A single shock front exists when the density gradient is positive (density increasing in the direction of impact), but two shocks can coexist when the density gradient is negative (density decreasing in the direction of impact) [9,11]. It should also be noted that the solution assumes that the response is governed by the shock deformation mechanism as is the case for impact velocities above a certain critical velocity [4,28] when the inertial effects associated with localized cell collapse dominate. The proposed closed-form expressions provide significant savings in computational time and effort. In general, they present a better description of the physical nature of the problem. Moreover, parametric studies can be performed efficiently with the help of explicit analytical solutions.

The differential equations governing the dynamic behavior are formulated using shock theory by considering CM as a continuum. A density-graded CM of mass m and length L is shown in Fig. 1. A rigid body of mass M strikes the CM at the incident end with an initial velocity V_0 and the other (transmitted) end of the CM is held stationary. The relative density varies linearly from $\overline{\rho}_i$ at the incident end to $\overline{\rho}_t$ at the transmitted end. The relative density $\overline{\rho}$ is expressed as the ratio of CM density (ρ) and solid material density (ρ_s).

A dimensionless density gradient parameter λ quantifying the gradation is defined as follows:

$$\lambda = \frac{\Delta\overline{\rho}}{2\overline{\rho}_0}, \tag{1}$$

where $\Delta\overline{\rho} = \overline{\rho}_t - \overline{\rho}_i$ is the difference between the relative densities at the two ends and $\overline{\rho}_0 = (\overline{\rho}_i + \overline{\rho}_t)/2$ is the average relative density. The linear variation in relative density along the length of the CM can be expressed as:

$$\overline{\rho} = \overline{\rho}_0\left[1 + \lambda\left(\frac{2X}{L} - 1\right)\right], \tag{2}$$

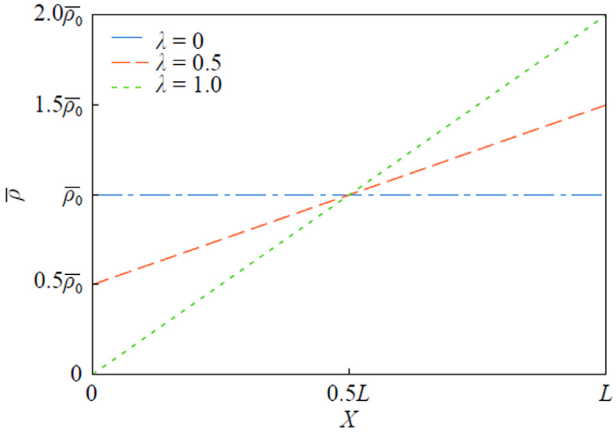

Fig. 2. Relative density variation.

where X is the undeformed position coordinate along the length of the CM. The density gradient parameter can have values ranging from -1 to 1, with the zero value corresponding to the uniform density. This study deals with only non-negative values of the density gradient parameter. Negative values of density gradient parameter result in double shock mode, which is out of the scope of the present study. The relative density variation for different density gradient parameters is shown in Fig. 2. Since the relative density cannot take negative values, density gradient parameter can be at most equal to one.

An RPPL material behavior, same as the idealization employed in previous studies [3,5,9,11], is used in the present study. The variation in the plateau stress σ_p and densification strain ϵ_d (sometimes also called as locking strain) with respect to the relative density $\overline{\rho}$ is given by the following equations [1]:

$$\sigma_p = \sigma_s C_1 \overline{\rho}^{C_2}, \tag{3}$$

$$\epsilon_d = C_3 - C_4\overline{\rho}, \tag{4}$$

where σ_s is the yield stress of the solid material and C_1, C_2, C_3 and C_4 are solid material parameters. Both the plateau stress and densification strain also vary along the length as they are dependent on the relative density. The parent material parameters C_1, C_2, C_3 and C_4 are often obtained from either experiments or numerical simulations. In previous studies, the value of C_2 has been taken to be 1.5 or 2 [1,9,10,29]. The parameter C_3 is taken equal to C_4 in some works [9] while both C_3 and C_4 are taken specifically equal to unity in some other works [11,13,30]. To maintain generality, the solution in the present study is determined without placing such restrictions on parent material parameters. Specific values are substituted after the solution expression is obtained.

The deformation of the CM after the rigid mass has moved by distance u is illustrated in Fig. 3. Both the undeformed and deformed configurations are shown in the figure. At this instant, the shock front has propagated towards the transmitted end by distance X_f, and its instantaneous velocity is V_{sf}. The region behind the shock front is compacted to length x_f, and it moves along with the rigid mass at the instantaneous velocity, V_f. The material ahead of the shock front of length X_u remains undeformed, and hence its velocity is zero. The total length of the CM in deformed configuration is l. The jump equations across the shock front are derived based on the conservation of mass and linear momentum in the Lagrangian form Ref. [31]. They are given by:

$$-\rho_f V_{sf}[\![1/\rho]\!] = [\![V]\!], \tag{5}$$

$$\rho_f V_{sf}[\![V]\!] = [\![\sigma]\!], \tag{6}$$

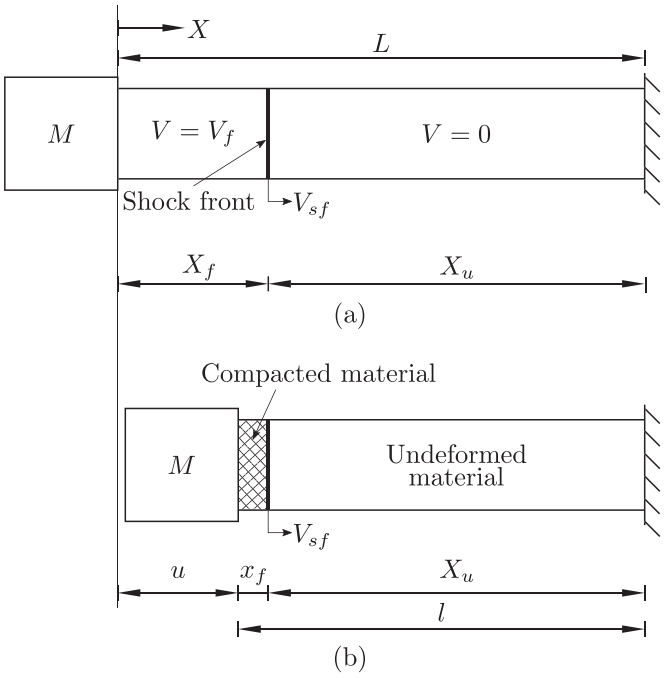

Fig. 3. Deformation in density-graded CM **a** undeformed configuration and **b** deformed configuration.

where ρ_f is the density just ahead of the shock front. The symbol $[\![\xi]\!] = \xi^+ - \xi^-$ denotes the change in physical quantity ξ across the shock front as it jumps from ξ^- to ξ^+. The superscripts - and + indicate the quantities just ahead of and behind the shock front, respectively. The compressive stress is taken to be positive in Eq. (6). The states of the material ahead of and behind the shock front are given by Eqs. (7) and (8), respectively.

$$\left\{\rho^-, \sigma^-, \epsilon^-, V^-\right\} = \left\{\rho_f, \sigma_{pf}, 0, 0\right\}, \tag{7}$$

$$\left\{\rho^+, \sigma^+, \epsilon^+, V^+\right\} = \left\{\rho_{df}, \sigma_{df}, \epsilon_{df}, V_f\right\}. \tag{8}$$

Eliminating V_{sf} from Eqs. (5) and (6), and using Eqs. (7) and (8) yields,

$$\left(\sigma_{df} - \sigma_{pf}\right)\left(1 - \frac{\rho_f}{\rho_{df}}\right) = \rho_f V_f^2. \tag{9}$$

The instantaneous strain ϵ_{df} behind the shock front is given by:

$$\epsilon_{df} = \frac{\mathrm{d}X_f - \mathrm{d}x_f}{\mathrm{d}X_f}, \tag{10}$$

where $\mathrm{d}X_f$ is an infinitesimal length of undeformed material compacting to length $\mathrm{d}x_f$ after the passage of shock. Note that the compressive strains are considered to be positive. Using conservation of mass, Eq. (10) can be written as:

$$\epsilon_{df} = 1 - \frac{\rho_f}{\rho_{df}}. \tag{11}$$

Combining Eqs. (9) and (11), the stress behind the shock is obtained.

$$\sigma_{df} = \sigma_{pf} + \frac{\rho_f V_f^2}{\epsilon_{df}}. \tag{12}$$

The conservation of linear momentum for the rigid mass and compacted region gives:

$$\sigma_{df} = -\left(\frac{M}{A} + \int_0^{X_f} \rho(X)\mathrm{d}X\right)\frac{\mathrm{d}V_f}{\mathrm{d}t}, \tag{13}$$

where A is the cross-sectional area of CM. Using Eqs. (5) and (11), it can be shown that the shock front velocity is given by:

$$V_{sf} = \frac{\mathrm{d}X_f}{\mathrm{d}t} = \frac{V_f}{\epsilon_{df}}. \tag{14}$$

The final differential equation was constructed with time as the independent variable in Refs. [9,11] and its solution was obtained numerically. However, in this work, to facilitate the analytical solution process, the differential equation is formulated with shock front position X_f as the independent variable. Therefore, using Eqs. (12)–(14) the following differential equation is derived:

$$\frac{\sigma_{pf}\epsilon_{df}}{V_f} + \rho_f V_f = -\left(\frac{M}{A} + \int_0^{X_f} \rho(X)\mathrm{d}X\right)\frac{\mathrm{d}V_f}{\mathrm{d}X_f}. \tag{15}$$

The following relations are used for non-dimensionalization:

$$\overline{X}_f = \frac{X_f}{L}, \overline{M} = \frac{M}{m}, \overline{\sigma}_{pf} = \frac{\sigma_{pf}}{\sigma_{p0}}, \overline{V}_f = \frac{V_f}{\sqrt{\sigma_{p0}/\rho_0}}, \tag{16}$$

where σ_{p0} is the plateau stress corresponding to the average density ρ_0, $m = \rho_0 AL$ is the mass of the CM, and $\overline{M}$ is the ratio of rigid mass and CM mass. The following is the dimensionless form of Eq. (15):

$$\frac{\overline{\sigma}_{pf}\epsilon_{df}}{\overline{V}_f} + \frac{\overline{\rho}_f}{\overline{\rho}_0}\overline{V}_f = -\left(\overline{M} + \frac{1}{\overline{\rho}_0}\int_0^{\overline{X}_f} \overline{\rho}\left(\overline{X}\right)\mathrm{d}\overline{X}\right)\frac{\mathrm{d}\overline{V}_f}{\mathrm{d}\overline{X}_f}. \tag{17}$$

Using $Y = \overline{V}_f^2$, Eq. (17) can be transformed to the following linear ordinary differential equation:

$$\frac{\mathrm{d}Y}{\mathrm{d}\overline{X}_f} + \frac{2H}{G}Y = \frac{-2F}{G}, \tag{18}$$

where the functions $F\left(\overline{X}_f\right)$, $G\left(\overline{X}_f\right)$ and $H\left(\overline{X}_f\right)$ defined to aid the solution are given as follows.

$$F\left(\overline{X}_f\right) = \overline{\sigma}_{pf}\epsilon_{df}, \tag{19}$$

$$G\left(\overline{X}_f\right) = \overline{M} + \frac{1}{\overline{\rho}_0}\int_0^{\overline{X}_f} \overline{\rho}\left(\overline{X}\right)\mathrm{d}\overline{X}, \tag{20}$$

$$H\left(\overline{X}_f\right) = \frac{\overline{\rho}_f}{\overline{\rho}_0}. \tag{21}$$

The solution to Eq. (18) is given by:

$$Y\left(\overline{X}_f\right) = \overline{V}_f^2 = (-Q + c)/P, \tag{22}$$

where c is a constant to be obtained from the initial conditions and the functions P and Q are given by the following equations:

$$P\left(\overline{X}_f\right) = \exp\left(\int \frac{2H}{G}\mathrm{d}\overline{X}_f\right), \tag{23}$$

$$Q\left(\overline{X}_f\right) = \int \left(\frac{2F}{G}P\right)\mathrm{d}\overline{X}_f. \tag{24}$$

The function G given by Eq. (20) can be evaluated by using Eq. (2), and its form in terms of λ is given by:

$$G\left(\overline{X}_f\right) = \overline{M} + \overline{X}_f\left[1 - \lambda\left(1 - \overline{X}_f\right)\right]. \tag{25}$$

Therefore, using Eq. (25), the integral in Eq. (23) can be simplified resulting in:

$$P = \exp\left(2\int \frac{\mathrm{d}G}{G}\right) = G^2. \tag{26}$$

Thus, Eq. (24) also reduces to:

$$Q = 2\int F G \mathrm{d}\overline{X}_f. \tag{27}$$

The integral in Eq. (27) can be evaluated depending on the value of λ. For $\lambda = 0$, the expression for Q takes a simpler form and is expressed as:

$$Q\left(\overline{X}_f\right) = \epsilon_{d0}\overline{X}_f\left(2\overline{M} + \overline{X}_f\right), \text{if } \lambda = 0, \tag{28}$$

where ϵ_{d0} is the densification strain corresponding to average density ρ_0. For $\lambda \neq 0$, using Eqs. (1)–(4), the integral in Eq. (27) can be written in terms of $\overline{\rho}_f$ leading to:

$$Q = \int \frac{C_1\sigma_s\overline{\rho}_f^{C_2}\left(C_3 - C_4\overline{\rho}_f\right)}{\sigma_{p0}}\left[\overline{M} + \frac{\overline{\rho}_f^2 - \overline{\rho}_0^2(1-\lambda)^2}{4\lambda\overline{\rho}_0^2}\right]\frac{\mathrm{d}\overline{\rho}_f}{\lambda\overline{\rho}_0}. \tag{29}$$

Further, the integral in Eq. (29) can be evaluated to the following form:

$$Q\left(\overline{X}_f\right) = \frac{\overline{\sigma}_{pf}}{4\lambda^2}\left\{\frac{\overline{\rho}_f}{\overline{\rho}_0}\left(\frac{C_3}{C_2+1} - \frac{C_4\overline{\rho}_f}{C_2+2}\right)\cdot\left[4\lambda\overline{M} - (1-\lambda)^2\right] + \frac{\overline{\rho}_f^3}{\overline{\rho}_0^3}\left(\frac{C_3}{C_2+3} - \frac{C_4\overline{\rho}_f}{C_2+4}\right)\right\}, \text{if } 0 < \lambda \leq 1. \tag{30}$$

It is important to note that Eq. (30) is not defined for $\lambda = 0$ and is only valid when $\lambda \neq 0$.

The constant c is determined from initial conditions. For $\overline{X}_f = 0$, $G = \overline{M}$ and $Y = \overline{V}_0^2$. Thus, c is given by:

$$c = \overline{M}^2\overline{V}_0^2 + Q(0). \tag{31}$$

Therefore, the final solution for V_f is obtained in terms of dimensionless functions $G\left(\overline{X}_f\right)$ and $Q\left(\overline{X}_f\right)$ as:

$$\overline{V}_f = \frac{1}{G\left(\overline{X}_f\right)}\sqrt{\overline{M}^2\overline{V}_0^2 - \left[Q\left(\overline{X}_f\right) - Q(0)\right]}, \tag{32}$$

where $Q(0)$ is the initial value of function Q, when the shock front is at the incident end. Thus, $Q(0)$ can be obtained by using $\overline{X}_f = 0$ and $\overline{\rho}_f = \overline{\rho}_i$. For $\lambda = 0$, the Eq. (32) after simplification is identical to that shown in the previous work for a uniform density CM [6]. However, Eq. (32) is more general and is applicable to CM with any linear non-negative density gradient including the specific case of uniform density. The function Q is determined by Eq. (28) or Eq. (30) depending on the value of the density gradient parameter.

The numerical solution is obtained with time as an independent variable similar to previous studies [9,11]. Thus, using Eq. (14), the differential equation given by Eq. (17) is transformed to:

$$\frac{\mathrm{d}\overline{V}_f}{\mathrm{d}\overline{t}} = -\left(\overline{\sigma}_{pf} + \frac{\overline{\rho}_f\overline{V}_f^2}{\overline{\rho}_0\epsilon_{df}}\right)\left[\overline{M} + \frac{1}{\overline{\rho}_0}\int_0^{\overline{X}_f}\overline{\rho}\left(\overline{X}\right)\mathrm{d}\overline{X}\right]^{-1}, \tag{33}$$

where $\overline{t} = \left(t\sqrt{\sigma_{p0}/\rho_0}\right)/L$. Equations (14) and (33) are used in discretized form to numerically calculate the instantaneous velocity of the rigid mass as a function of shock front location. Forward finite difference method is used to obtain the solution.

The comparison of the velocity of the rigid mass obtained from Eq. (32) with the numerical solutions is shown in Fig. 4. The plots are shown for $\overline{V}_0 = 1$ and $\overline{V}_0 = 2$. Unless otherwise stated, the following representative values are used for the calculations: $\overline{\rho}_0 = 0.15$, $\overline{M} = 1$, $C_2 = 2$, $C_3 = 1$, $C_4 = 1$ and $\lambda = 0.5$. With $\overline{V}_0 = 1$, the input kinetic energy supplied is not sufficient to propagate the shock front to the transmitted end. The rigid mass comes to rest and the CM remains partially compacted (see Fig. 4a). The error in the numerical solution is shown in Fig. 4b. One of the drawbacks of the numerical solution is that the accuracy of the solution is dependent on the time step $\delta\overline{t}$. Often multiple iterations are required for determining the time step that will yield sufficiently accurate results. It is observed in the figure that the numerical solution slowly converges to the analytical solution as the time step is reduced. The reduction in time step size only increases the computational time. The error due to the finite time step is small in the beginning, but it accumulates with shock front propagation and is maximum in the end. The error is only shown up to $\overline{X}_f = 0.6$ in Fig. 4b because it increases dramatically as the velocity approaches zero. Figure 4c shows the case when $\overline{V}_0 = 2$. In this case, the input energy is more than the minimum energy required for the full compaction of CM. Therefore, the shock front propagates to the other end as seen in the figure, and the velocity of the rigid mass, in the end, remains non-zero even after full compaction of CM. The error in the numerical solution decreases with smaller step sizes (see Fig. 4d) same as the case observed for $\overline{V}_0 = 1$.

There exists an initial velocity of the impinging mass whose associated kinetic energy is just sufficient to compact the CM completely and at the same time, the impinging mass comes to rest. This initial velocity is denoted as densification velocity and is obtained by substituting $\overline{V}_f = 0$ at $\overline{X}_f = 1$ in Eq. (32). The dimensionless densification velocity is given by:

$$\overline{V}_d = \frac{\sqrt{Q(1) - Q(0)}}{\overline{M}}. \tag{34}$$

The input kinetic energy is dissipated by the compaction of CM. The kinetic energy associated with the densification velocity is called the densification energy, and it is equal to the EA capacity of CM according to the principle of conservation of energy. The specific EA capacity is the EA capacity per unit mass of the CM. Thus, the analytical expression for the dimensionless specific EA capacity $\overline{E}_d$ is given by:

$$\overline{E}_d = \frac{1}{2}\overline{M}\,\overline{V}_d^2 = \frac{Q(1) - Q(0)}{2\overline{M}}. \tag{35}$$

The specific EA capacity is shown in Fig. 5a and the error in the numerical solutions in Fig. 5b. It is clearly seen that the numerical solutions can be misleading if an appropriate time step is not used. A coarser time step ($\delta\overline{t} = 1\times10^{-2}$) shows an initial decreasing trend as opposed to the monotonically increasing trend shown by the analytical solution in Fig. 5a. It is also observed that the density gradation improves the EA capacity. The energy absorption occurs through plastic dissipation, and it is greatly enhanced by the shock deformation mechanism when the compaction velocity is high. Note that the compaction velocity is high during the early stage of deformation, and it gradually decreases due to energy absorption. The overall mass of the graded CMs is the same as that of the uniform density CM. However, in graded CMs, the mass is distributed by placing the low-density material towards the incident end and the high-density material towards the transmitted end. The low-density material compacts at high velocity, absorbing more energy due to the shock deformation mechanism. As the CM gets compacted further, the high-density material towards the transmitted end experiences lower velocities resulting in lower energy absorption by the shock deformation mechanism. However, the high density of the material ensures a significant amount of plastic dissipation owing to its high plateau stress. Thus, the variation in density along the length helps in effectively absorbing energy throughout the compaction process. Therefore the overall energy absorption capacity is enhanced in a density-graded CM over the uniform density CM, and the enhancement is maximum for the steepest density gradient.

The incident stress is the stress exerted on the rigid mass by the CM. It is obtained by applying conservation of linear momen-

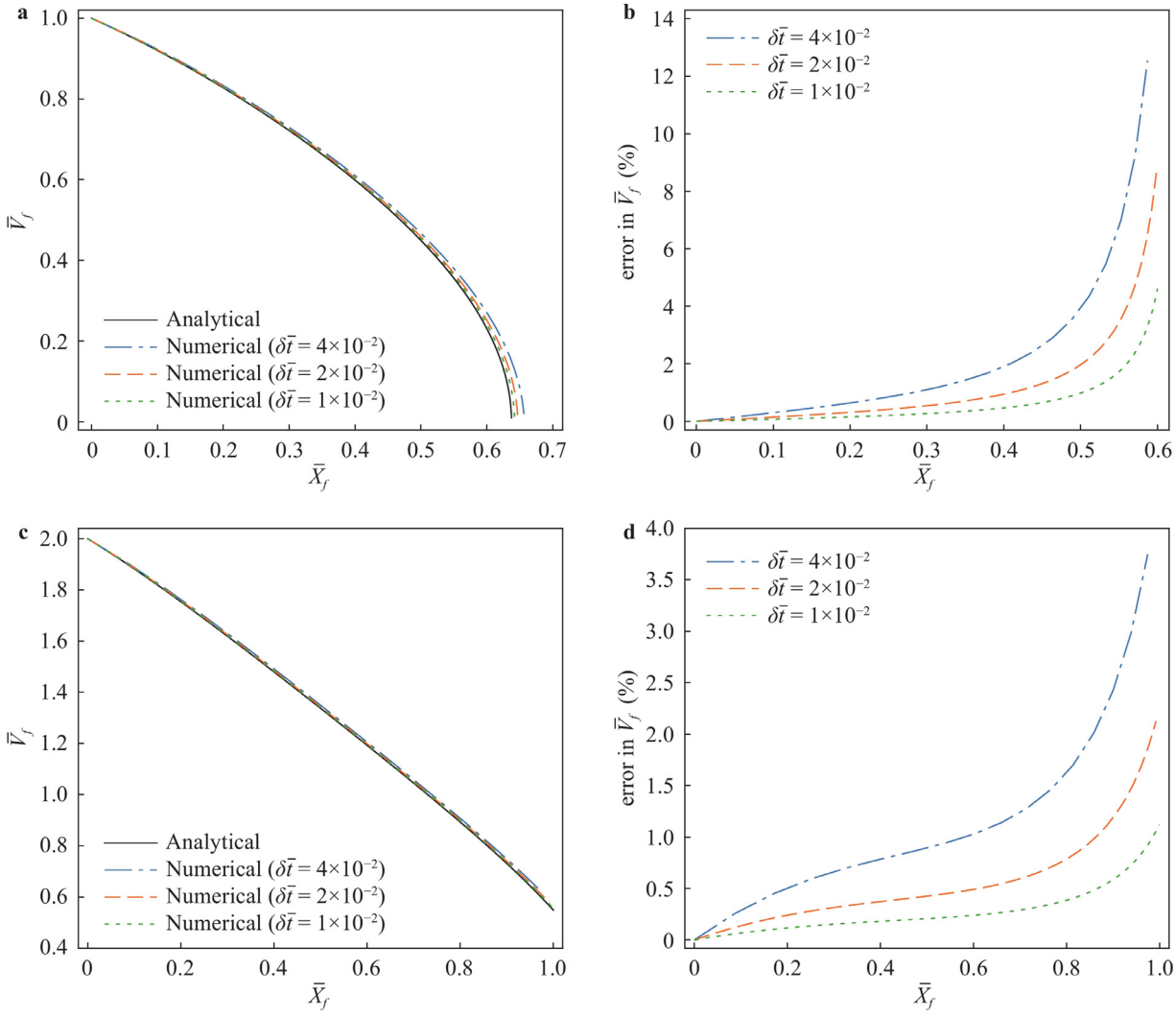

Fig. 4. Instantaneous velocity $\bar{V}_f$ of the rigid mass as a function of $\bar{X}_f$, **a** $\bar{V}_f$ when $\bar{V}_0 = 1$, **b** error in $\bar{V}_f$ when $\bar{V}_0 = 1$, **c** $\bar{V}_f$ when $\bar{V}_0 = 2$, **d** error in $\bar{V}_f$ when $\bar{V}_0 = 2$.

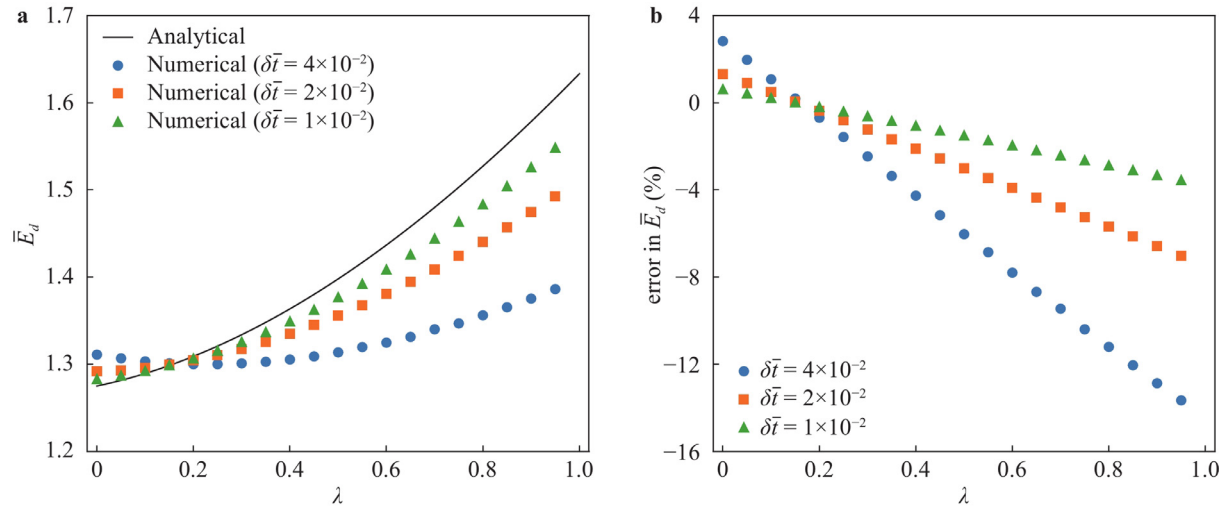

Fig. 5. **a** Specific EA capacity $\bar{E}_d$ as a function of λ; **b** error in specific EA capacity $\bar{E}_d$.

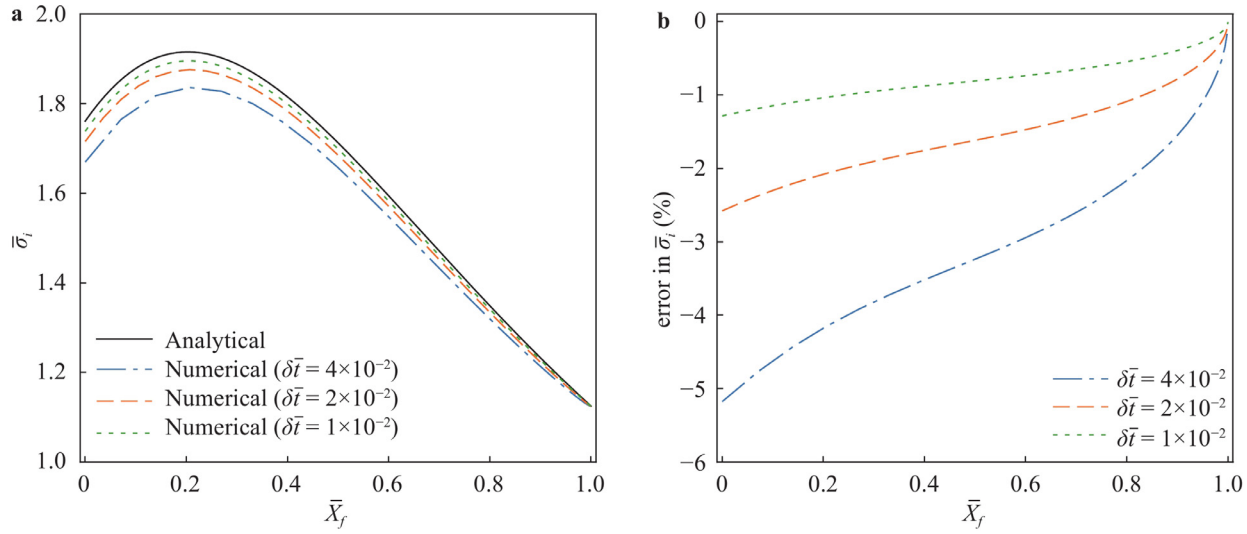

Fig. 6. **a** Dimensionless incident stress $\bar{\sigma}_i$ as a function of $\bar{X}_f$; **b** error in dimensionless incident stress $\bar{\sigma}_i$.

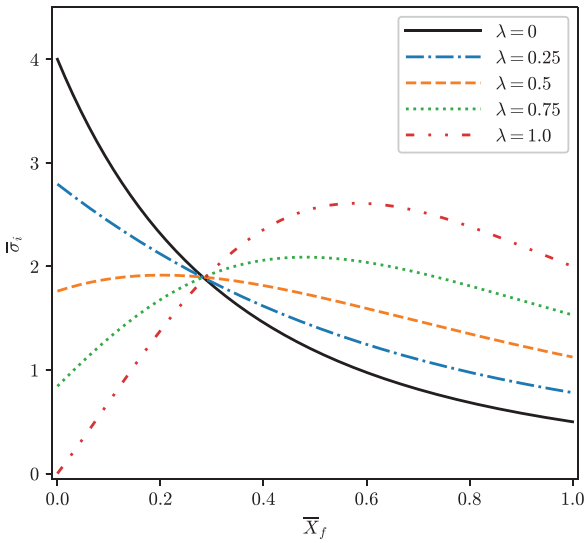

Fig. 7. Dimensionless incident stress $\bar{\sigma}_i$ for different density gradient parameters.

tum to the rigid mass and is expressed as:

$$\sigma_i = -\frac{M}{A}\frac{\mathrm{d}V_f}{\mathrm{d}t}. \tag{36}$$

Using Eqs. (12), (13), (20) and (36), the dimensionless incident stress is obtained as:

$$\bar{\sigma}_i = \frac{\bar{M}}{G}\left(\bar{\sigma}_{pf} + \frac{\bar{\rho}_f \bar{V}_f^2}{\bar{\rho}_0 \epsilon_{df}}\right). \tag{37}$$

The dimensionless incident stress is shown in Fig. 6a for $\bar{V}_0 = \bar{V}_d$ and $\lambda = 0.5$ along with the error in Fig. 6b. The analytical solution shows a good agreement, as before, with the numerical solution. Figure 7 shows the incident stress obtained analytically for different density gradient parameters. The peak incident stress occurs at $\bar{X}_f = 0$ for $\lambda = 0$ and $\lambda = 0.25$. However, for higher values of λ, it does not occur at $\bar{X}_f = 0$. This is because the density near the incident end is low enough, resulting in smaller plateau stress and larger densification strain. All these factors (see Eq. (37)) lead to lower incident stress at $\bar{X}_f = 0$ despite compaction at high velocity. In the later stage, as the density of the compacting material increases, the velocity also remains sufficiently high. Therefore, the incident stress increases and reaches a peak value at some location. In the end, since the velocity ($\bar{V}_f$) becomes zero, the incident stress drops to a lower value. Both the location and the magnitude of the peak incident stress are dependent upon the density gradient parameter. This also indicates that the incident stress profile can be designed by choosing a suitable density gradient parameter. This is an extremely useful characteristic that can be exploited when designing impact-resistant structures. Figure 8 shows the dimensionless peak incident stress $\bar{\sigma}_i^{\text{peak}}$ as a function of λ. It is observed that the peak incident stress is minimum around $\lambda = 0.55$. Very high values of λ lead to higher peak incident stress. This is because, for CM with very high λ, the velocity does not drop much after the low-density material near the incident end has compacted. Afterward, the compaction of high-density material at high velocities causes higher peak incident stress.

The theoretical analysis for the stationary graded CM impacted by a rigid mass is presented in this study. RPPL material behavior is assumed, and linear density gradients are considered. An analytical approach that leads to closed-form solutions is demonstrated. Expressions for the velocity of the rigid mass, densification velocity, energy absorption capacity, and incident stress are determined. The proposed solution captures the dynamic behavior of the material with great accuracy. The comparison of analytical results with the numerical solutions validates the accuracy and efficiency of the derived expressions. The analytical solution shows that the density gradation improves the energy absorption capacity, and the enhancement is maximum when the density gradient parameter is maximum. Also, the peak incident stress is observed to be minimum at intermediate values of the density gradient parameter. The effect of each variable on the behavior of CM under impact loading can be determined using the proposed analytical expressions. The solution can also be used to predict the dynamic response of the naturally occurring density-graded CM such as a human skull [32,33]. Furthermore, it could be adapted for modeling a multilayer structure with discrete values of densities by using a piecewise function for density variation. More importantly, the proposed analytical formulation can be a fast and efficient tool, in general, to design graded CMs for impact mitigation.

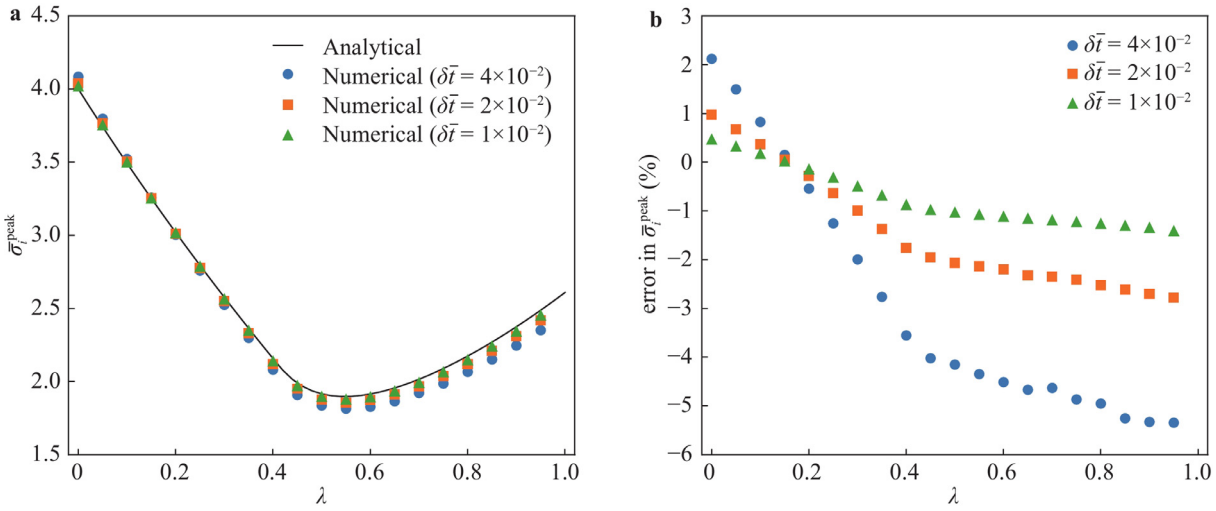

Fig. 8. **a** Dimensionless peak incident stress $\bar{\sigma}_i^{peak}$ as a function of λ; **b** error in dimensionless peak incident stress $\bar{\sigma}_i^{peak}$

Declaration of Competing Interest

The authors declare that they have no known competing financial interests or personal relationships that could have appeared to influence the work reported in this paper.

Credit authorship contribution statement

Vijendra Gupta: Conceptualization, Methodology, Formal analysis, Writing –original draft. Addis Kidane: Supervision, Writing – review & editing. Michael Sutton: Supervision, Writing –review & editing.

Acknowledgment

The authors are grateful for the the financial support provided by the US Army Research Office under grant number W911NF-18-1-0023.

References

[1] L.J. Gibson, M.F. Ashby, Cellular Solids, Cambridge Solid State Science Series, Second, Cambridge University Press, 1997, doi:10.1017/CBO9781139878326. URL: https://www.cambridge.org/core/product/identifier/9781139878326/type/book.

[2] Y. Sun, Q.M. Li, Dynamic compressive behaviour of cellular materials: a review of phenomenon, mechanism and modelling, International Journal of Impact Engineering 112 (2018) 74–115, doi:10.1016/j.ijimpeng.2017.10.006.

[3] S. Reid, C. Peng, Dynamic uniaxial crushing of wood, International Journal of Impact Engineering 19 (1997) 531–570, doi:10.1016/S0734-743X(97)00016-X. URL: http://linkinghub.elsevier.com/retrieve/pii/S0734743X9700016X.

[4] P.J. Tan, S.R. Reid, J.J. Harrigan, Dynamic compressive strength properties of aluminium foams. Part I - experimental data and observations, Journal of the Mechanics and Physics of Solids 53 (2005) 2174–2205, doi:10.1016/j.jmps.2005.05.007.

[5] P.J. Tan, S.R. Reid, J.J. Harrigan, Dynamic compressive strength properties of aluminium foams. Part II - 'shock' theory and comparison with experimental data and numerical models, Journal of the Mechanics and Physics of Solids 53 (2005) 2206–2230, doi:10.1016/j.jmps.2005.05.003.

[6] J.J. Harrigan, S.R. Reid, A. Seyed Yaghoubi, The correct analysis of shocks in a cellular material, International Journal of Impact Engineering 37 (2010) 918–927, doi:10.1016/j.ijimpeng.2009.03.011.

[7] L. Cui, S. Kiernan, M.D. Gilchrist, Designing the energy absorption capacity of functionally graded foam materials, Materials Science and Engineering: A 507 (2009) 215–225, doi:10.1016/j.msea.2008.12.011. URL: https://linkinghub.elsevier.com/retrieve/pii/S0921509308013646.

[8] S. Kiernan, M.D. Gilchrist, Towards a virtual functionally graded foam: Defining the large strain constitutive response of an isotropic closed cell polymeric cellular solid, International Journal of Engineering Science 48 (2010) 1373–1386, doi:10.1016/J.IJENGSCI.2010.09.004. URL: https://www.sciencedirect.com/science/article/pii/S0020722510001886.

[9] X. Wang, Z. Zheng, J. Yu, Crashworthiness design of density-graded cellular metals, Theoretical and Applied Mechanics Letters 3 (2013) 031001, doi:10.1063/2.1303101.

[10] C.J. Shen, T.X. Yu, G. Lu, Double shock mode in graded cellular rod under impact, International Journal of Solids and Structures 50 (2013) 217–233, doi:10.1016/j.ijsolstr.2012.09.021.

[11] C.J. Shen, G. Lu, T.X. Yu, Investigation into the behavior of a graded cellular rod under impact, International Journal of Impact Engineering 74 (2014) 92–106, doi:10.1016/j.ijimpeng.2014.02.015.

[12] D. Karagiozova, M. Alves, Propagation of compaction waves in cellular materials with continuously varying density, International Journal of Solids and Structures 71 (2015) 323–337, doi:10.1016/j.ijsolstr.2015.07.005.

[13] H. Liu, Z. Zhang, H. Liu, et al., Theoretical investigation on impact resistance and energy absorption of foams with nonlinearly varying density, Composites Part B: Engineering 116 (2017) 76–88, doi:10.1016/j.compositesb.2017.02.012.

[14] P. Wang, X. Wang, Z. Zheng, Stress distribution in graded cellular materials under dynamic compression, Latin American Journal of Solids and Structures 14 (2017) 1251–1272, doi:10.1590/1679-78253428.

[15] A. Ajdari, H. Nayeb-Hashemi, A. Vaziri, Dynamic crushing and energy absorption of regular, irregular and functionally graded cellular structures, International Journal of Solids and Structures 48 (2011) 506–516, doi:10.1016/j.ijsolstr.2010.10.018.

[16] C.J. Shen, G. Lu, T.X. Yu, Dynamic behavior of graded honeycombs - a finite element study, Composite Structures 98 (2013) 282–293, doi:10.1016/j.compstruct.2012.11.002.

[17] J. Zhang, Z. Wang, L. Zhao, Dynamic response of functionally graded cellular materials based on the voronoi model, Composites Part B: Engineering 85 (2016) 176–187, doi:10.1016/j.compositesb.2015.09.045. URL: https://linkinghub.elsevier.com/retrieve/pii/S1359836815005892.

[18] D. Chen, S. Kitipornchai, J. Yang, Dynamic response and energy absorption of functionally graded porous structures, Materials and Design 140 (2018) 473–487, doi:10.1016/j.matdes.2017.12.019.

[19] Y. Li, Z. Feng, L. Hao, et al., A review on functionally graded materials and structures via additive manufacturing: From multi-scale design to versatile functional properties, Advanced Materials Technologies 5 (2020) 1900981, doi:10.1002/admt.201900981.

[20] B. Koohbor, S. Ravindran, A. Kidane, Impact response of density graded cellular polymers, Conference Proceedings of the Society for Experimental Mechanics Series 1 (2018) 17–23, doi:10.1007/978-3-319-62956-8_4.

[21] D. Miller, V. Gupta, A. Kidane, Dynamic response of layered functionally graded polyurethane foam with nonlinear density variation, Dynamic Behavior of Materials (2020) 25–30, doi:10.1007/978-3-030-30021-0_5.

[22] V. Gupta, D. Miller, A. Kidane, Numerical and experimental investigation of density graded foams subjected to impact loading, Dynamic Behavior of Materials (2020) 31–35, doi:10.1007/978-3-030-30021-0_6.

[23] B. Koohbor, S. Ravindran, A. Kidane, In situ deformation characterization of density-graded foams in quasi-static and impact loading conditions, International Journal of Impact Engineering 150 (2021) 103820, doi:10.1016/j.ijimpeng.2021.103820. URL: https://linkinghub.elsevier.com/retrieve/pii/S0734743X21000075.

[24] J. Liu, B. Hou, F. Lu, A theoretical study of shock front propagation in the density graded cellular rods, International Journal of Impact Engineering 80 (2015) 133–142, doi:10.1016/j.ijimpeng.2015.02.001. URL: https://linkinghub.elsevier.com/retrieve/pii/S0734743X15000160.

[25] J. Yang, S. Wang, Y. Ding, Crashworthiness of graded cellular materials: A design strategy based on a nonlinear plastic shock model, Materials Science and Engineering: A 680 (2017) 411–420, doi:10.1016/j.msea.2016.11.010. URL: https://linkinghub.elsevier.com/retrieve/pii/S0921509316313715.

[26] B. Chang, Z. Zheng, Y. Zhang, Crashworthiness design of graded cellular materials: an asymptotic solution considering loading rate sensitivity, International Journal of Impact Engineering 143 (2020) 103611, doi:10.1016/j.ijimpeng.2020.103611. URL: https://linkinghub.elsevier.com/retrieve/pii/S0734743X19313995.

[27] V. Gupta, D. Miller, A. Kidane, Optimization for improved energy absorption and the effect of density gradation in cellular materials, 2021, 13-20, doi:10.1007/978-3-030-59765-8_4.

[28] P.J. Tan, J.J. Harrigan, S.R. Reid, Inertia effects in uniaxial dynamic compression of a closed cell aluminium alloy foam, Materials Science and Technology 18 (2002) 480–488, doi:10.1179/026708302225002092.

[29] S.K. Maiti, L.J. Gibson, M.F. Ashby, Deformation and energy absorption diagrams for cellular solids, Acta Metallurgica 32 (1984) 1963–1975, doi:10.1016/0001-6160(84)90177-9.

[30] H. Liu, Z. Zhang, H. Liu, Effect of elastic target on Taylor-Hopkinson impact of low-density foam material, International Journal of Impact Engineering 94 (2016) 109–119, doi:10.1016/j.ijimpeng.2016.04.005. URL: https://linkinghub.elsevier.com/retrieve/pii/S0734743X16301944.

[31] L. Davison, Fundamentals of Shock Wave Propagation in Solids, Shock Wave and High Pressure Phenomena, Springer Berlin Heidelberg, Berlin, Heidelberg, 2008, doi:10.1007/978-3-540-74569-3.

[32] Q. Wu, L. Ma, Q. Liu, Impact response and energy absorption of human skull cellular bones, Journal of the Mechanical Behavior of Biomedical Materials 81 (2018) 106–119, doi:10.1016/j.jmbbm.2018.02.018. URL: https://linkinghub.elsevier.com/retrieve/pii/S175161611830170X.

[33] Q. Wu, C. Yang, A. Ohrndorf, Impact behaviors of human skull sandwich cellular bones: Theoretical models and simulation, Journal of the Mechanical Behavior of Biomedical Materials 104 (2020) 103669, doi:10.1016/j.jmbbm.2020.103669. URL: https://linkinghub.elsevier.com/retrieve/pii/S1751616119315735.